Optical Test

Application Brief

Metrology in Production Environments

QPSI™ Data Acquisition

Phase-shifting interferometry (PSI) is the gold standard in optical metrology; it is widely used for precision measurements of optical surface form and profiling. However, PSI is susceptible to errors caused by environmental influences. The desire to have metrology in the production work cell can be challenging due to vibration generated by optical manufacturing equipment. This often limits the ability to perform accurate phase shifting acquisition requiring a user to either accept a less accurate visual interpretation method or use an expensive and more complex dynamic solution.

To solve this problem, ZYGO has developed QPSI, an easy to use vibration robust acquisition solution that maintains the accuracy of a true-Fizeau interferometer configuration. Combined with a complementary hardware configuration, the patented QPSI algorithm quantifies the rigid body motion of the cavity and compensates for the vibration in each subsequent acquisition. This allows each frame to be individually validated, eliminating the dependency that occurs in traditional PSI where all frames of a multi-bucket acquisition must occur in a sufficiently stable environment.

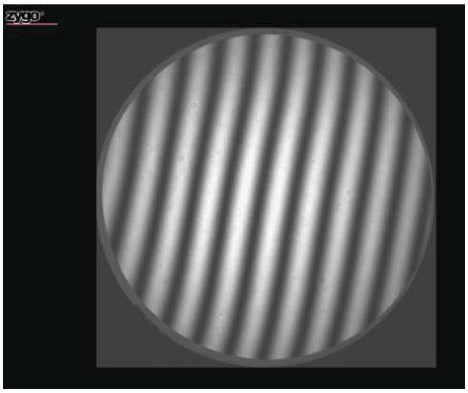

Live Display

Live Display shows the presence of several tilt fringes.

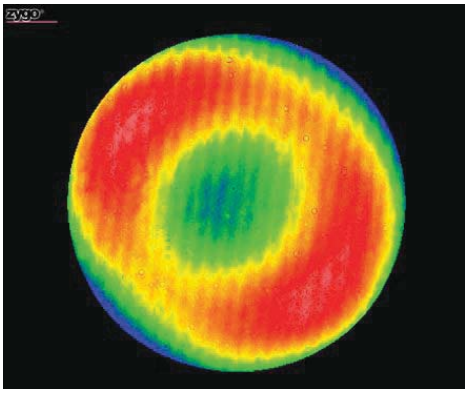

PSI

Using PSI, vibration can cause fringe print-through on the data.

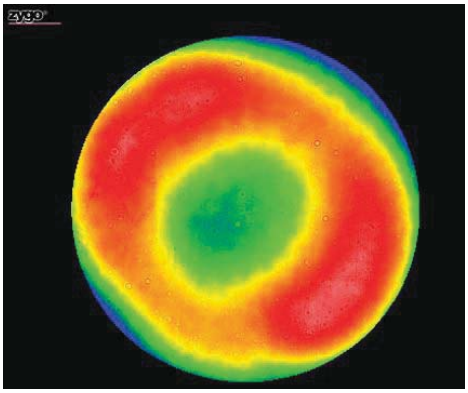

QPSI

QPSI eliminates ripple and print-through without vibration isolation.

Why ZYGO?

QPSI provides an easy to use method to enable accurate and cost effective surface form metrology on the production floor. This patented technique is the only vibration robust, true-Fizeau solution that allows for phase measuring acquisition in vibration prone environments – in most cases without the need for an isolation table.

With over 40 years of metrology experience, Zygo Corporation continues to strengthen its reputation as the world's premier supplier of non-contact optical measuring instrumentation.

zygo

AMETEK
ULTRA PRECISION TECHNOLOGIES

AB-0102 10/14

Distribution in the UK & Ireland

Lambda

Characterisation, Measurement & Analysis

Lambda Photometrics Limited
Lambda House Batford Mill
Harpenden Herts AL5 5BZ
United Kingdom
E: info@lambdaphoto.co.uk
W: www.lambdaphoto.co.uk
T: +44 (0)1582 764334
F: +44 (0)1582 712084

Model-based phase shifting interferometry

Leslie L. Deck

Zygo Corporation, Laurel Brook Rd., Middlefield, Connecticut 06455, USA (LDeck@zygo.com)

Received 24 April 2014; accepted 27 May 2014;
posted 6 June 2014 (Doc. ID 210809); published 11 July 2014

A general method of surface profiling with phase-shifting interferometry techniques uses iterative linear regression to fit the sequence of interferograms to a physical model of the cavity. The physical model incorporates all important cavity influences, including environmentally induced rigid-body motion, phase shifter miscalibrations, multiple interference, geometry-induced spatial phase-shift variations, and their cross-couplings. By incorporating an initial estimate of the surface profile and iteratively solving for space- and time-dependent variables separately, convergence is robust and rapid. The technique has no restriction on surface shape or departure. © 2014 Optical Society of America

OCIS codes: (120.3180) Interferometry; (120.3940) Metrology; (120.5050) Phase measurement; (120.6650) Surface measurements, figure; (120.7280) Vibration analysis.
http://dx.doi.org/10.1364/AO.53.004628

1. Introduction

Phase-shifting interferometry (PSI) [1] is a powerful tool in optical metrology, widely used for precision measurements of optical wavefronts and surface profiling. In profiling applications, the surface under test is part of an optical cavity and illuminated to produce an interference pattern (interferogram) between wavefronts reflected from the test and reference surfaces of the cavity. Analysis of the intensity variation from a sequence of phase-shifted interferograms taken while modulating the cavity's optical path difference (OPD) determines the wavefront phase. The spatial map of these phases represents the modulo-2π OPD between the two surfaces of the cavity, which relates back to the physical surface topography using the illumination wavelength and the known reference surface topography.

The number of interferograms in the sequence, their phase spacing (phase-shift increment), and the algorithm coefficients determine the performance characteristics of the algorithm against a variety of error sources, including errors in the phase-shift increment (detuning error), multiple reflections, and environmental influences like vibration [2]. Modern PSI algorithms address these error sources but nonetheless assume a known phase-shift increment [1], making them susceptible to disturbances that change this value. Additionally, cross coupling between different error sources remains a limitation to PSI performance [3].

The model-based PSI or MPSI technique described in this paper [4–6] fits the interferogram sequence to a mathematical model that includes all, or at least the most important, physical variations that occur during the acquisition. In principle, this approach can handle all major error sources and their cross coupling as long as the model correctly includes their influence and sufficient information is obtained in the acquisition to adequately decouple the contributions. The resulting coupled, nonlinear model equations cannot be solved directly, so the approach is to linearize the model and apply iterative least-squares (LS) techniques. Though this approach has been considered before [7–12], the large number of unknowns has made efficient solutions difficult, producing unreliable or slow convergence or requiring restricted physical models that do not account for many important effects. No previous work has been general enough to account for all of the influences mentioned above and their cross couplings.

This model-based approach is applicable to any interferometer type; however in this paper I describe

1559-128X/14/214628-09$15.00/0

MPSI applied specifically to precision measurements with a mechanically phase-shifted laser Fizeau interferometric profiler, a common surface profiling tool. For this application the goal is not to achieve environmental immunity but rather to reach a higher level of performance under conditions found in standard practice. The method assumes the presence of, and attempts to improve upon, an initial phase map produced from an initial PSI measurement. In this regard, it is similar to the vibration compensation (VC) method described in a previous publication [13]; however, unlike VC, MPSI can account for most physical effects and their coupled interactions naturally. The benefits of having the initial phase map include improved convergence, excellent correction over a large variety of errors, and no restrictions on surface shape or interferometer type.

I first detail the mathematical model and iteration sequence and then use simulated data examples to highlight the major points and verify the performance. Real data examples follow to illustrate significant improvements under realistic conditions.

2. MPSI Applied to Mechanically Phase-Shifted Fizeau Interferometers

Figure 1 depicts a typical PSI measurement system using a Fizeau optical geometry. A piezoelectric transducer moves the reference surface along the Z axis in a known manner while a digital camera with N pixels images the object so that each camera pixel corresponds to a unique position on the object surface. The camera samples the cavity interference at discrete times t_j with $j = 1 \ldots F$ so that F camera frames are acquired with nominal phase shifts corresponding to those desired by the chosen PSI algorithm. Camera shuttering is employed to eliminate motion-induced contrast blurring.

The mathematical model applied to this cavity assumes that the reference surface is a low-reflectivity dielectric (glass), and the cavity is restricted to rigid body motion, both typically excellent approximations. The interference signal between the wavefronts reflected from the test and reference surfaces is given by the familiar Airy formula,

$$I(\mathbf{x}, t) = \left| \frac{\sqrt{r_{\text{ref}}} + \sqrt{r_{\text{test}}}\, \exp[i\Theta(\mathbf{x}, t)]}{1 + \sqrt{r_{\text{ref}} r_{\text{test}}}\, \exp[i\Theta(\mathbf{x}, t)]} \right|^2, \tag{1}$$

where r_{ref} and r_{test} are the reference and test intensity reflectivity magnitudes and $\Theta(\mathbf{x}, t)$ is the optical phase delay between the two surfaces at image location (pixel) $\mathbf{x}$ and time t. Note that here and in what follows, the time variable is understood to be discretely sampled, so explicitly subscripting the time variable with j is suppressed. A Fourier series expansion of this formula to order K is

$$I(\mathbf{x}, t) = A(\mathbf{x}) + V(\mathbf{x}) \sum_{k=1}^{K} (-g)^{k-1} \cos[k\Theta(\mathbf{x}, t)], \tag{2}$$

where $A(\mathbf{x})$ and $V(\mathbf{x})$ are the DC and interference contrast intensity terms, respectively, and $g = \sqrt{r_{\text{ref}} r_{\text{test}}}$. Typical laser Fizeau glass reference surfaces have an intensity reflectivity of $r_{\text{ref}} \approx 4\%$, so the series can be terminated at the $\cos(3\Theta)$ term with less than 1% intensity error even for a $r_{\text{test}} \approx 90\%$. Cavity motions are modeled through the definition of Θ:

$$\Theta(\mathbf{x}, t) = \Phi(\mathbf{x}) + \Delta(\mathbf{x}, t), \tag{3}$$

where $\Phi(\mathbf{x})$ is the cavity phase map evaluated at time t_0, and $\Delta(\mathbf{x}, t)$ describes the various processes that modify the optical phase:

$$\Delta(\mathbf{x}, t) = \varphi(t_0) + \alpha(t)x + \beta(t)y + [\varphi(t) - \varphi(t_0)]\sqrt{1 - \rho(\mathbf{x})^2 c^2}, \tag{4}$$

where $\varphi(t)$ is the time variation of the phase shift along the Z axis, $\alpha(t)$ and $\beta(t)$ are the two orthogonal rigid-body tilt coefficients, $\rho(\mathbf{x})^2 = x^2 + y^2$, c is the phase curvature, and time t_0 represents the point in the phase shift for which the phase map is evaluated—often the first frame in the sequence. The last term in Δ accounts for the spatial dependence of the phase shift when mechanically shifting a spherical cavity along the Z axis [14] and can be significant in fast spherical cavities. This term is absent for a plano cavity (since $c = 0$) or if mechanical phase shifting is replaced with wavelength tuning.

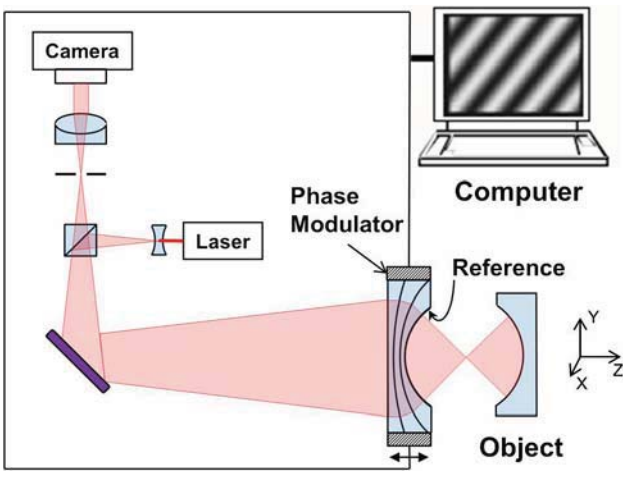

Fig. 1. Typical laser Fizeau interferometer system configured to measure a sphere.

3. Initial Estimates and Iteration

The mathematical model given by Eqs. (2) and (3) accounts for all the error sources mentioned in the introduction but is highly coupled and nonlinear. The model contains three time-independent unknowns $A(\mathbf{x})$, $V(\mathbf{x})$, and $\Phi(\mathbf{x})$, three time-dependent unknowns $\varphi(t)$, $\alpha(t)$, and $\beta(t)$, and two unknown constants c and g, for a total of $3N + 3F + 2$ unknowns, which can easily run into the millions considering the pixel density of modern cameras. Ultimately, it is the phase map $\Phi(\mathbf{x})$ that is interesting for profiling

applications and separating the time-dependent and time-independent unknowns is an efficient solution path. To this end, an iterative scheme alternately solves for the time-dependent unknowns and then the time-independent ones using linearized versions of the model.

The process begins by acquiring initial estimates for $A(\mathbf{x})$, $V(\mathbf{x})$, and $\Phi(\mathbf{x})$. These estimates need not be of high quality and are relatively easy to produce. For example, $A(\mathbf{x})$ and $V(\mathbf{x})$ are initially estimated with

$$\begin{aligned} A(\mathbf{x}) &= \{\max[I_m(\mathbf{x},t)] + \min[I_m(\mathbf{x},t)]\}/2 \\ V(\mathbf{x}) &= \{\max[I_m(\mathbf{x},t)] - \min[I_m(\mathbf{x},t)]\}/2, \end{aligned} \tag{5}$$

where $I_m(\mathbf{x},t)$ is a measured intensity, and both the max() and min() functions operate over all interferograms in the acquired sequence. The requirement of an initial phase map $\Phi(\mathbf{x})$ might seem to be a weak point; however, recall that we are interested in improving on PSI performance for typical applications, not achieving vibration immunity. There are many options for obtaining the initial phase map estimate, and the choice can influence the MPSI convergence depending on how closely the initial phase map reflects the true profile. Following [13], this paper uses a PSI algorithm applied to some fraction of the interferogram sequence to obtain an initial $\Phi(\mathbf{x})$, and this choice turns out to be quite adequate in a large variety of applications.

Treating the initial estimates for the time-independent variables as constant, fitting each interferogram in the sequence to a linearized form of the mathematical model provides new estimates for the time-dependent variables and the curvature c. Writing

$$\begin{aligned} \varphi_n(t) &= \varphi(t) + \varphi'(t) \\ \alpha_n(t) &= \alpha(t) + \alpha'(t) \\ \beta_n(t) &= \beta(t) + \beta'(t) \\ c_n &= c + c', \end{aligned} \tag{6}$$

where the subscript n denotes a new estimate and a prime represents small deviations from the current value, a straightforward linearization to the first order in the deviations means the new intensity can be written as

$$\begin{aligned} I_n(\mathbf{x},t) = I(\mathbf{x},t) + \cdots \\ + [\varphi'(t)\gamma(\mathbf{x}) + \alpha'(t)x + \beta'(t)y + c'\eta(\mathbf{x},t)]H(\mathbf{x},t), \end{aligned} \tag{7}$$

with

$$H(\mathbf{x},t) = -V(\mathbf{x}) \sum_{k=1}^{K} (-g)^{k-1} k \, \sin[k\Theta(\mathbf{x},t)], \tag{8}$$

and

$$\begin{aligned} \gamma(\mathbf{x}) &= \sqrt{1 - \rho(\mathbf{x})^2 c^2} \\ \eta(\mathbf{x},t) &= -[\varphi(t) - \varphi(t_0)]\rho(\mathbf{x})^2 c/\gamma(\mathbf{x}). \end{aligned} \tag{9}$$

Since Eq. (7) is linear in the deviations, standard linear regression techniques apply. The merit function $\chi(t)$,

$$\chi(t) = \frac{1}{2M} \sum_{i=1}^{M} \left[\frac{I_m(\mathbf{x}_i,t) - I_n(\mathbf{x}_i,t)}{V(\mathbf{x}_i)} \right]^2, \tag{10}$$

serves both as a data quality and minimization metric, and the sum is over a set of M spatial locations with $M \le N$. The merit function is normalized by the contrast so that the maximum value when integrated over 2π of phase is 1. Once the deviations are found, the time-dependent variables are updated with Eq. (6).

The time-dependent variables are then treated as constant when determining new estimates for the time-independent variables $A(\mathbf{x})$, $V(\mathbf{x})$, and $\Phi(\mathbf{x})$. To this end, the coefficients of the different interference orders are solved directly and independently by rewriting Eq. (2) as

$$\begin{aligned} I(\mathbf{x},t) = A(\mathbf{x}) + \sum_{k=1}^{K} C_k(\mathbf{x}) \cos[k\Delta(\mathbf{x},t)] \\ + \sum_{k=1}^{K} S_k(\mathbf{x}) \sin[k\Delta(\mathbf{x},t)], \end{aligned} \tag{11}$$

with

$$\begin{aligned} C_k(\mathbf{x}) &= V(\mathbf{x})(-g)^{k-1} \cos[k\Phi(\mathbf{x})] \\ S_k(\mathbf{x}) &= -V(\mathbf{x})(-g)^{k-1} \sin[k\Phi(\mathbf{x})]. \end{aligned} \tag{12}$$

Equation (11) is linear in $A(\mathbf{x})$, $C_k(\mathbf{x})$, and $S_k(\mathbf{x})$, so again standard LS techniques can be applied for each of the M spatial locations, but now each is processed along the time axis. The original time-independent variables are recovered with

$$\begin{aligned} V(\mathbf{x}) &= \sqrt{C_1(\mathbf{x})^2 + S_1(\mathbf{x})^2} \\ \Phi(\mathbf{x}) &= \tan^{-1}[-S_1(\mathbf{x})/C_1(\mathbf{x})], \end{aligned} \tag{13}$$

and if the interference model order (K) is greater than one, a new estimate for g follows from

$$g = \frac{\sum_{i=1}^{M} \sqrt{C_2(\mathbf{x}_i)^2 + S_2(\mathbf{x}_i)^2}}{\sum_{i=1}^{M} V(\mathbf{x}_i)}. \tag{14}$$

Although not explicitly shown here for brevity, weighting factors to the various LS fits can account for data quality. The merit function inverse $\chi(t)^{-1}$ in

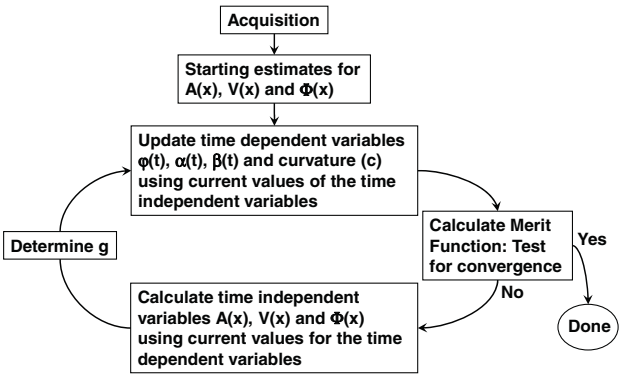

Fig. 2. MPSI process flow.

particular can be a useful data quality metric for the time-independent fits. Iterating between solving for the time-dependent and time-independent variables continues until a termination condition is satisfied. Figure 2 depicts this measurement process flow.

Though this procedure involves significant computation, spatially subsampling the interferogram field to a set of M spatial locations substantially reduces the computation time. Typically a few thousand uniformly distributed spatial locations is sufficient, representing less than 1% of the total number of pixels in modern imagers. In this way, the overall processing speed is increased by a factor of 100 or more. MPSI also converges quickly, often requiring 10 or fewer iterations. There are two main reasons for the rapid convergence: the availability of a starting phase map and the separation of the time-dependent and time-independent solutions. The result is that a typical MPSI analysis completes in a fraction of a second using modern personal computers.

4. Method Performance—Simulations

Unlike PSI or VC, the iterative nature of MPSI makes it difficult to derive analytic formulas for environmental sensitivity, so simulations were used to evaluate MPSI performance over a large range of cavity, environmental, and acquisition conditions.

A. Convergence

In general, the simulations show the algorithm converges to the correct surface profile as long as two conditions are met:

1. Intensity information is available over a broad enough range of optical phases.
2. Environmental conditions are not so extreme that the initial phase map fails catastrophically.

The first condition underscores the fact that phase extraction using a LS method from a limited set of intensities distributed about the unit circle is most robust if the complete circle (the full 2π range of phases) is sampled, since that minimizes the possibility of degenerate solutions. This concept is called phase diversity [13], and sampling the full unit circle implies a phase diversity of 2π. All phase extraction algorithms attempt to maximize phase diversity with a limited set of samples.

The second condition is a consequence of using a PSI algorithm to produce the initial phase map, which determines the surface phase through the arctangent of the ratio of two filtered intensity sequences [1]. Catastrophic failures in PSI algorithms occur in two ways: (1) the vibration shifts the signal outside the filter band-pass, causing indeterminate phases and giving rise to data dropouts, or (2) the vibration changes the phase-shift direction, producing a π phase discontinuity across fringe orders.

Alternative methods of acquiring a starting phase map do not suffer from these failure modes. An example is the rapid acquisition of two adjacent interferograms in quadrature which, along with the DC estimate, provides an initial phase map with significantly less sensitivity to harsh environmental conditions but requires additional hardware [15,16]. In another case, two arbitrary frames in relative quadrature (plus the DC estimate) are used, with the phase sign determined by correlating the phase shifts with the known imparted phase-shift sequence [17]. In this variant, the vibration performance improves with the number of interferograms acquired.

A convenient and useful iteration termination condition is that the fractional change in the frame merit function $\chi(t)$ [Eq. (10)] between iterations falls below a certain threshold—typically 0.1% is chosen. Figure 3 shows a typical plot of the mean of this termination metric (averaged over all interferograms) versus iteration number. The fractional merit function change drops by almost an order of magnitude per iteration at the beginning of the loop, converging rapidly to changes of less than 1% in about 6 iterations. The figure shows that a termination metric threshold of 0.1% is sufficient to achieve

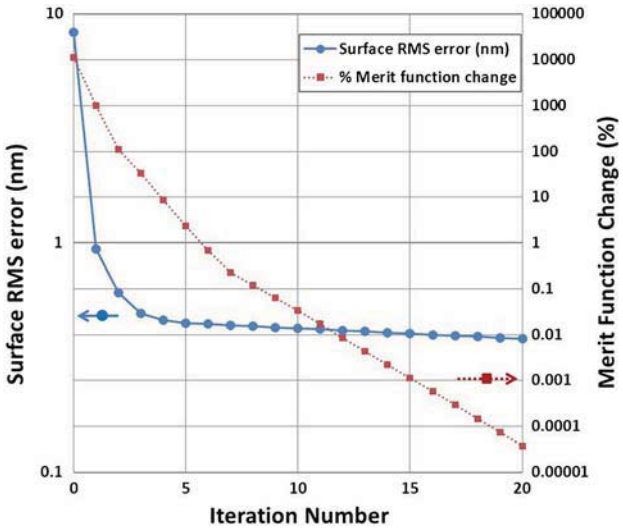

Fig. 3. Typical plot of the surface RMS error and the mean merit function change as a function of the number of iterations. A merit function change threshold of 0.1% is typically used as an iteration termination condition. The arrows indicate which axis to use for which curve.

subnanometer-level surface profiles, and the process typically terminates in less than 10 iterations.

B. Vibration Performance

A significant feature of MPSI is its ability to account for all rigid body motions of the surfaces that make up the cavity. In general, MPSI accounts well for environmental vibrations as long as the convergence conditions mentioned in the previous section are satisfied. Compared to plano cavities, mechanically phase-shifted spherical cavities have an additional variable (the phase curvature c), and the last term in $\Delta(\mathbf{x}, t)$ requires knowing the total phase-shift difference between interferograms measured between time t and t_0 (the point in the phase shift for which the phase map is evaluated). Since the phases are measured modulo-2π, an additional phase unwrapping step is required, creating errors in the last term if any phase increment exceeds π. These additional considerations make spherical cavities more susceptible to vibrations than plano cavities.

The two convergence conditions imply that MPSI vibration performance in this paper is primarily linked to the vibration performance of the PSI algorithm chosen for the initial phase map. It is straightforward to estimate the vibration amplitude required to violate the first condition, at least for pure piston vibrations. Figure 4 shows this amplitude (in nanometers) as a function of vibrational frequency for a well-known 13-frame PSI algorithm [18]. Numerical simulation shows the greatest amplitude restrictions at vibrational frequencies of ¼ and ¾ of the frame rate. However, even at those frequencies, vibration amplitudes up to ~70 nm can be accommodated, representing quite a severe vibration for typical applications.

To illustrate a number of performance features of MPSI, Fig. 5 represents the residual measurement error maps (difference between true and measured surfaces) derived from simulations with a challenging cavity configuration—a fast spherical cavity with moderately high finesse under various vibration conditions. The test surface form was modeled as a sphere with a 40% reflectivity and a departure of three fringes to make it easier to observe the residual error. The surface form and cavity configuration is nominally similar to one of the real samples measured in Section 6. Thirteen mechanically phase-shifted interferograms (500 × 500 pixels) with nominally 45° phase increments were generated for a numerical aperture of 0.77 (equivalent to an F/0.65 transmission sphere) and analyzed with conventional PSI. This PSI result was then used as the initial phase map for the MPSI analysis, which used a 0.1% termination threshold and an interference order (K) equal to 3. The surface error maps for pure sinusoidal piston vibrations at three different vibration amplitudes are shown; 0, 20, and 60 nm. The vibration frequency corresponded to the frequency for which the PSI algorithm has the greatest sensitivity (¼ of the frame rate). The simulations included 8-bit intensity digitization and 1 bit of normally distributed random intensity noise. A HeNe wavelength

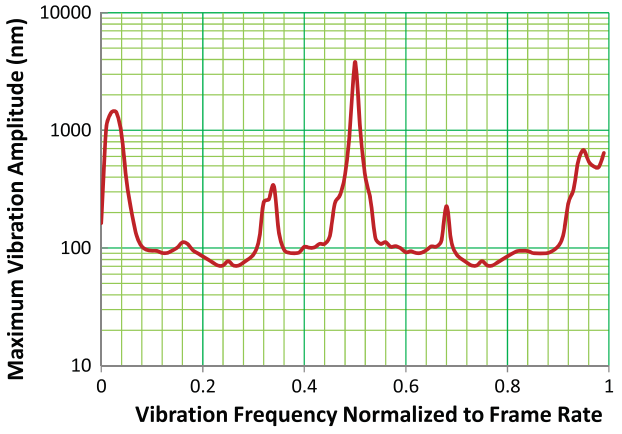

Fig. 4. Maximum allowed pure piston vibration amplitude for convergence as a function of vibration frequency normalized to the frame rate when using the 13-frame algorithm.

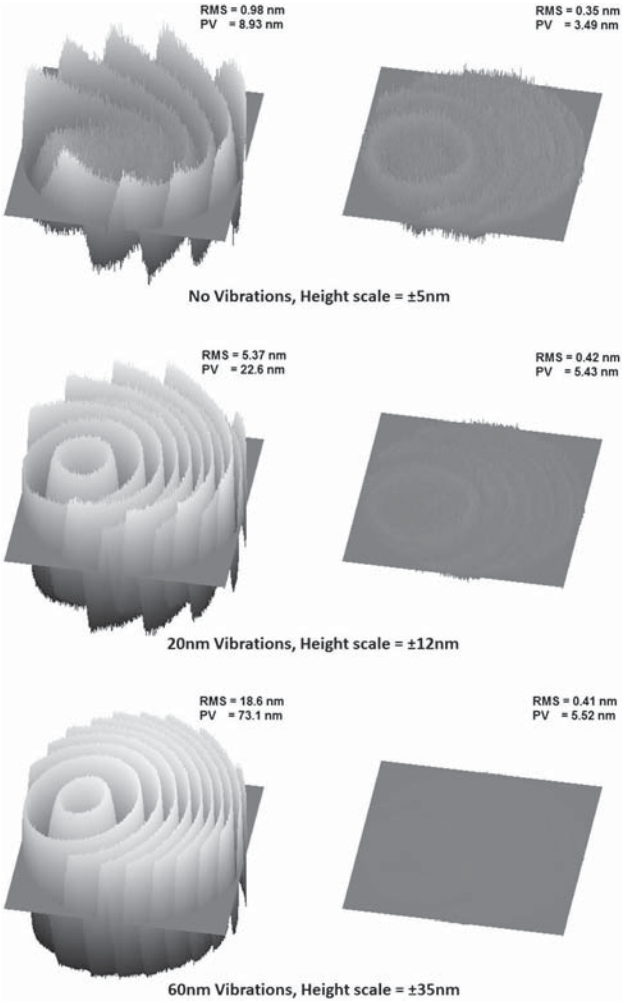

Fig. 5. Surface error maps for conventional PSI (left column) and MSPI (right column) from simulations of a 4%–40% fast spherical cavity with no vibrations (top), 20 nm amplitude vibrations (middle), and 60 nm amplitude vibrations (bottom). Note the different height scales.

(633 nm) was assumed when translating the phase error into nanometers.

First note that the PSI result has a measurable error even when vibrations are absent. The errors are due to cross coupling between the cavity finesse and spatially dependent detuning caused by mechanical phase-shifting [3]. As expected, the largest errors occur at the edges of the field where the illumination angles are greatest, producing a peak-valley error of about 9 nm even in perfectly quiet conditions.

As the vibration amplitude increases, the vibrational error surpasses the cross-coupling error in PSI so the residual error profile is dominated by the two-cycle "ripple" characteristic of vibration disturbances. For PSI, the RMS surface error at 60 nm vibration amplitude is almost 20× higher than the quiescent result. In contrast, the MSPI-derived surface is not significantly affected by the cavity finesse, the spatially dependent phase shift variation, or vibration amplitude and exhibits essentially the identical surface map under all conditions with an RMS error close to the theoretically expected value from intensity uncertainty alone (0.30 nm).

5. Factors that Can Influence Performance

The model described in Section 2 includes many of the influences found in standard practice but is not comprehensive. Furthermore it makes certain assumptions that will be violated to some degree in real-world applications. This section calls attention to these model deficiencies and describes their effect on the final surface profile.

A. Air Turbulence

The model specifically assumes the cavity surfaces respond as rigid bodies to environmental influences. With regard to mechanical vibrations, this is an excellent approximation, certainly for the objects typically profiled with PSI techniques and vibration amplitudes considered in this paper. Air turbulence, however, is not considered. Air turbulence introduces errors in the calculated rigid-body parameters, which in turn produce globally incorrect phase shifts. Thus, spatially localized turbulence with a specific amplitude introduces a smaller amplitude distortion with a spatial frequency content that depends on the surface departure. Since turbulence is usually stochastic, the standard remedy is to average enough measurements to reduce the residual error below a required value. For extreme vibration or turbulent conditions, instantaneous measurement methods, for example carrier fringe methods, may be more appropriate [19].

B. Starting Phase Map

For plane cavities (or spherical cavities measured with wavelength tuning methods), the quality of the starting phase map influences the convergence rate but does not prevent convergence to the correct profile as long as the convergence conditions in Section 4.A are satisfied. Generally, spherical cavities act similarly, but the added curvature variable and additional phase unwrapping step needed to calculate the last term in Eq. (4) can lead to cases where MPSI converges to an incorrect profile, particularly if the phase diversity is small. The probability of this occurrence decreases rapidly as the available phase diversity increases, making it relatively rare in practice.

C. Temporal Intensity Fluctuations

Both the PSI calculation for the initial phase map and the MPSI model assume the illumination intensity is constant over the acquisition time. Deviations from this introduce error in the contrast and DC maps and ultimately the surface profile. The form of the error generally depends on the surface departure, producing a ripple distortion with the same spatial frequency content as the interference. The illumination in well-designed PSI systems is usually stable enough so this effect is negligible; however, the addition of a single intensity monitor acquired simultaneously with the main camera can provide enough information to correct for intensity fluctuations if required.

D. Nonlinear Intensity Transfer Function

Ideally, the camera converts intensity into a perfectly proportional electric signal; however, this is never perfect for real cameras. Well-designed PSI systems use cameras with linearity typically better than 0.1%, so this effect is usually negligible; however, look-up tables can restore the linearity to acceptable levels if necessary.

E. Retrace Error

Retrace error is the additional optical path length associated with beams that are imperfectly retroreflected from the test surface, and so all real surfaces exhibit some level of retrace error. The degree of retrace distortion depends sensitively on the optical characteristics of the interferometer and the amount of wavefront departure. Retrace error does not directly influence MPSI performance, and since MPSI works well with low phase diversity, surfaces can be measured under cavity conditions that minimize this error.

6. Real Examples

This section demonstrates typical measurement results of precision optical surfaces under a variety of environmental conditions using Zygo VeriFire XPZ and QPZ interferometers. MPSI performance was tested on both flat and spherical cavities for a variety of vibration conditions.

Figures 6 and 7 compare conventional PSI and MPSI surface profiles for two representative measurements made on plane and spherical objects, respectively. In both cases pure piston vibrations were applied with amplitudes of ~60 nm (1.19 rad) with a normalized frequency set to the most sensitive part of the PSI sensitivity spectrum (1/4 of the

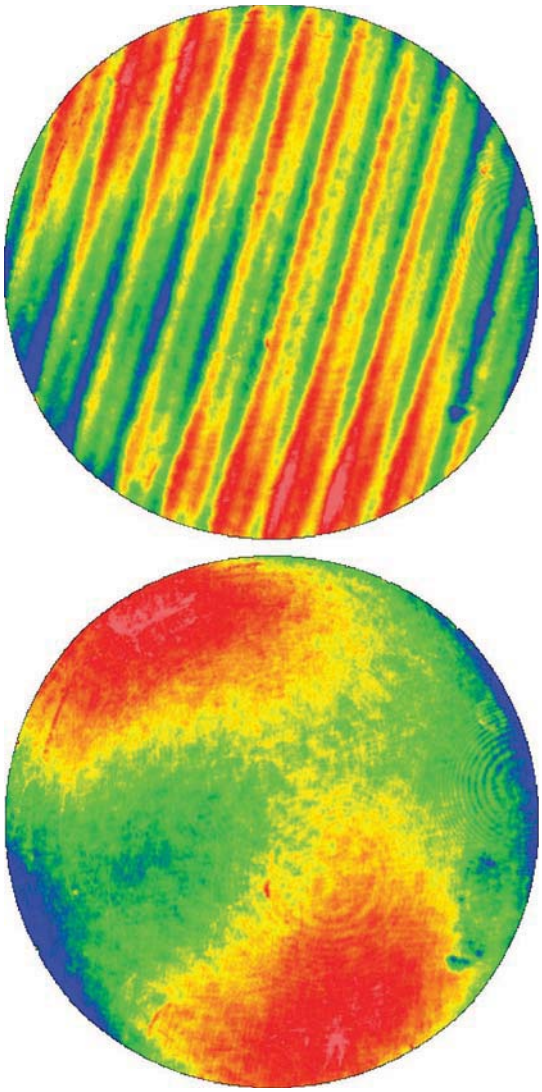

Fig. 6. Top profile represents a conventional PSI measurement of a vibrated flat cavity with about five fringes of tilt. The bottom profile shows the same data set processed with MPSI.

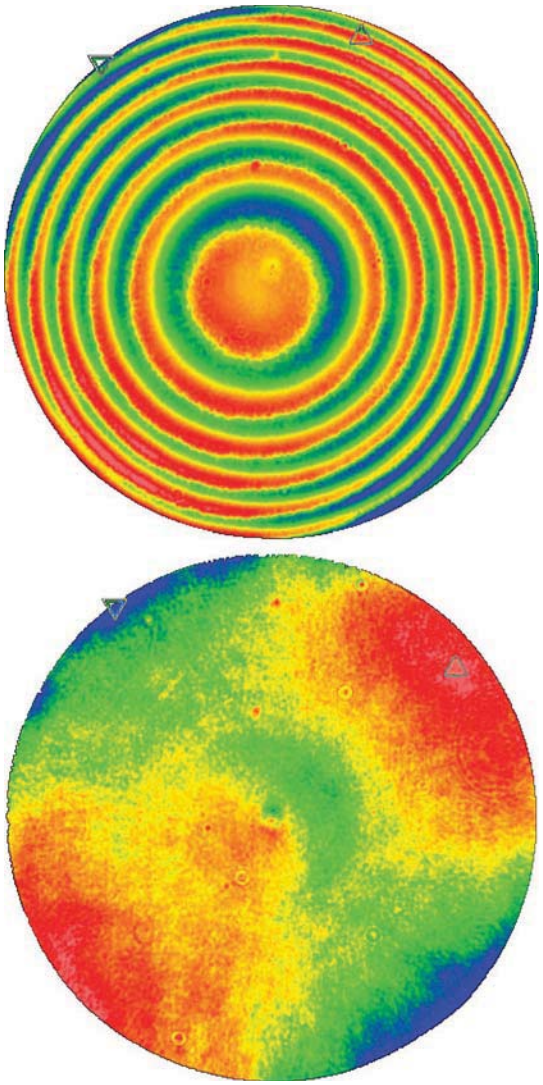

Fig. 7. Top profile represents a conventional PSI measurement of a vibrated spherical cavity with four fringes of departure. The bottom profile shows the same data set processed with MPSI.

camera frame rate). The large-amplitude ripple distortion evident in the PSI measured profiles is absent after MPSI is applied. The PSI profile was used as the starting phase map in both cases. These two profiles were calculated from the identical data sets used to demonstrate the VC method [13] and show that MPSI performance is at least equal to VC for these two piston-only vibrational disturbances.

Figure 8 is an example of MPSI performance for a cavity undergoing large combined piston and tilt motions, where applying VC was less successful. The top plot shows the PSI-determined phase map. As is typical of tilt motions, the "ripple" distortion amplitude from a PSI analysis is field dependent since the phase shifts vary spatially. Additionally, the environment was severe enough to be close to violating the convergence conditions of Section 4.A, which are manifested as data dropouts. These dropouts occur during the spatial phase unwrapping step in the PSI measurement due to branch discontinuities caused by poorly determined phases. Again, the PSI phase map was used as the initial phase map for the MPSI analysis. In this case, enough of the PSI generated phase map survived for MPSI to work with, and the analysis accounts for the cavity motions well enough to significantly reduce phase noise and recover all of the surface data. This particular analysis converged in 12 iterations.

Measurements of a fast, high-reflective spherical cavity under quiet conditions illustrate how MPSI handles error cross coupling. The cavity consisted of a SiC sphere (40% reflectivity) illuminated through an F/0.65 transmission sphere. The cavity was intentionally set off-null by a few fringes to highlight the cross-coupling error, which follows the fringe pattern since it depends on the starting phase. The simulation results displayed in Fig. 5 used a similar surface form and cavity configuration.

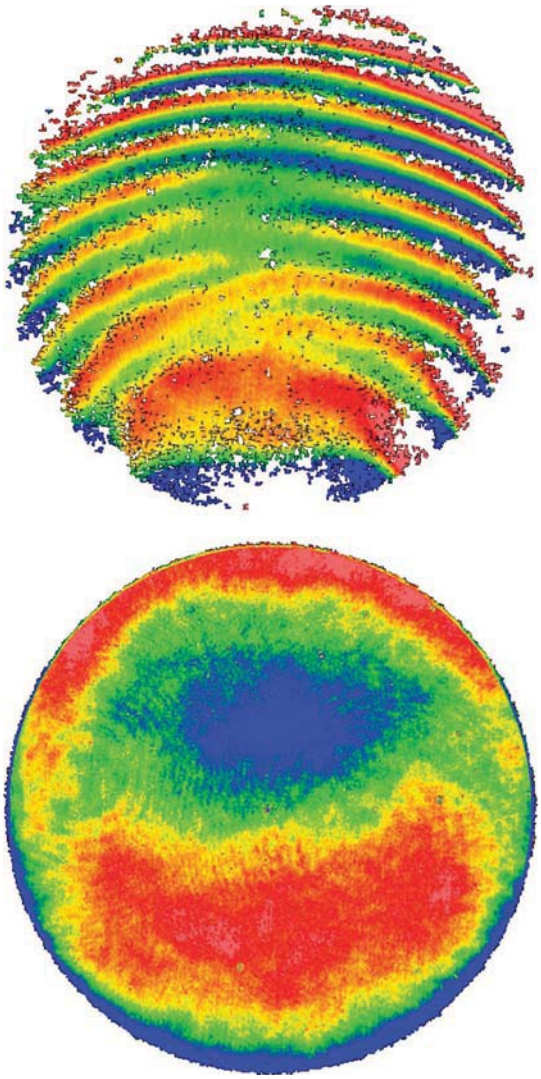

Fig. 8. Surface profiles from a 4%–4% cavity measured with an F/0.65 transmission sphere undergoing large tilt and piston motions. The top profile is the surface using conventional PSI, exhibiting ripple and data loss from phase breakup. The bottom profile shows the same surface after MPSI processing.

The real SiC surface departed sufficiently from a perfect sphere that simple sphere subtraction was ineffective in exposing the cross-coupling errors due to the residual form departure. To cancel out the nominal surface form more effectively and highlight these errors, differences between PSI and MPSI surface profiles are used. The left graph of Fig. 9 displays this difference profile for the simulated cavity (this graph is identical to the top-left graph of Fig. 5, but looking normally at the surface), and the right graph displays the profile difference from the real cavity. The color scales used in the two graphs were identical and set to ±5 nm. Both difference profiles are similar in both shape and magnitude. As one expects from cross-coupling error, the greatest departure occurs at the field edges and follows the interference phase. The mean ripple error at the field edge has a PV of 8–9 nm in both cases (the larger PV observed in the real data is due to a few single-point

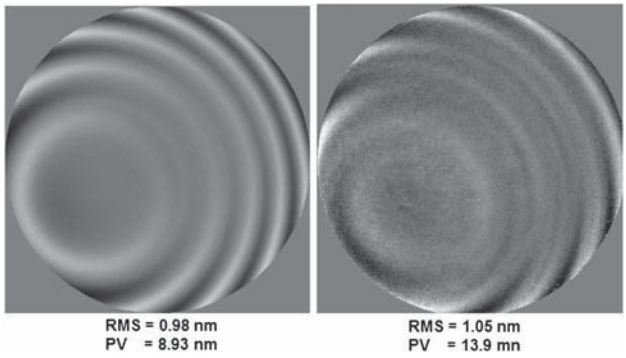

Fig. 9. Graphs of differences between PSI and MPSI surfaces from a 4%–40% fast (F/0.65) spherical cavity under quiet conditions for simulated (left) and real (right) data used to highlight the cross-coupling error. The color scale is set to ±5 nm in both graphs.

outliers). Less than 0.5 nm of departure is observed near the center (along the optical axis). The agreement between real data and simulation results provides strong support for the assertion that MPSI accounts well for these cross-coupling terms.

7. Summary

This paper describes an iterative LS approach to PSI accounting for most of the important physical effects that occur during the intensity acquisition, such as multiple interference, rigid-body surface motions, spatial and temporal phase-shift variations, environmental vibrations, and cross coupling between them. A mathematical model accounts for all of these physical processes, and iterative linear regression techniques are used to find the cavity variables that best fit the model. Iteration convergence is aided by the presence of a PSI-created initial estimate of the surface profile and by separately solving for the space- and time-domain variables. Convergence is robust, and typically fewer than 10 iterations provide subnanometer profile accuracy. The technique can be applied to interferometers of all types and has no restriction on surface shape or departure.

References and Notes

1. H. Schreiber and J. Bruning, "Optical shop testing," in *Phase Shifting Interferometry*, D. Malacara, ed., 3rd ed. (Wiley, 2007), Chap. 14.
2. P. de Groot, "Vibration in phase shifting interferometry," J. Opt. Soc. Am. A **12**, 354–365 (1995).
3. P. de Groot, "Correlated errors in phase shifting laser Fizeau interferometry," Appl. Opt. **53**, 4334–4342 (2014).
4. The techniques described in this paper are protected by U.S. patents 7,796,273, 7,796,275, 7,948,639, and foreign patents or patents pending.
5. L. Deck, "Phase shifting interferometry in the presence of vibration," U.S. patent 7,948,639 (24 May 2011).
6. The technique described in this paper is marketed by Zygo Corporation under the name QPSI.
7. I. Kong and S. Kim, "General algorithm for phase-shifting interferometry by iterative least-squares fitting," Opt. Eng. **34**, 183–187 (1995).
8. K. Okada, A. Sato, and J. Tsujiuchi, "Simultaneous calculation of phase distribution and scanning phase shift in phase shifting interferometry," Opt. Commun. **84**, 118–124 (1991).

9. G. S. Han and S. W. Kim, "Numerical correction of reference phases in phase-shifting interferometry by iterative least-squares fitting," Appl. Opt. **33**, 7321–7325 (1994).
10. M. Chen, H. Guo, and C. Wei, "Algorithm immune to tilt phase-shifting error for phase-shifting interferometers," Appl. Opt. **39**, 3894–3898 (2000).
11. Z. Wang and B. Han, "Advanced iterative algorithm for phase extraction of randomly phase-shifted interferograms," Opt. Lett. **29**, 1671–1673 (2004).
12. Q. Liu, Y. Wang, F. Ji, and J. He, "A three-step least-squares iterative method for tilt phase-shift interferometry," Opt. Express **21**, 29505–29515 (2013).
13. L. Deck, "Suppressing phase errors from vibration in phase shifting interferometry," Appl. Opt. **48**, 3948–3960 (2009).
14. P. de Groot, "Phase shift calibration errors in interferometers with spherical Fizeau cavities," Appl. Opt. **34**, 2856–2863 (1995).
15. P. Wizinowich, "Phase shifting interferometry in the presence of vibration: a new algorithm and system," Appl. Opt. **29**, 3271–3279 (1990).
16. L. Deck, "Phase shifting interferometry in the presence of vibration," U.S. patent 7,796,273 (14 September 2010).
17. L. Deck, "Phase shifting interferometry in the presence of vibration using phase bias," U.S. patent 7,796,275 (14 September 2010).
18. P. de Groot, "Measurement of transparent plates with wavelength-tuned phase-shifting interferometry," Appl. Opt. **39**, 2658–2663 (2000).
19. D. M. Sykora and M. L. Holmes, "Dynamic measurements using a Fizeau interferometer," Proc. SPIE **8082**, 80821R (2011).